

Title:**Automated Materials Discovery Platform Realized: Scanning Probe
Microscopy of Combinatorial Libraries****Authors:**

Yu Liu^{1*}, Rohit Pant², Ichiro Takeuchi², R. Jackson Spurling³, Jon-Paul Maria³, Maxim Ziatdinov⁴, and Sergei V. Kalinin^{1,4*}

¹ Department of Materials Science and Engineering, University of Tennessee, Knoxville, Tennessee, 37996, USA

² Department of Materials Science and Engineering, University of Maryland, College Park, Maryland 20742, USA

³ Materials Science and Engineering Department, Materials Research Institute, the Pennsylvania State University, University Park, Pennsylvania, 16802, USA

⁴ Physical Sciences Division, Pacific Northwest National Laboratory, Richland, Washington, 99354, USA

Abstract:

Combinatorial libraries are a powerful approach for exploring the evolution of physical properties across binary and ternary cross-sections in multicomponent phase diagrams. Although the synthesis of these libraries has been developed since the 1960s and expedited with advanced laboratory automation, the broader application of combinatorial libraries relies on fast, reliable measurements of concentration-dependent structures and functionalities. Scanning Probe Microscopies (SPM), including piezoresponse force microscopy (PFM), offer significant potential for quantitative, functionally relevant combi-library readouts. Here we demonstrate the implementation of fully automated SPM to explore the evolution of ferroelectric properties in combinatorial libraries, focusing on Sm-doped BiFeO₃ and Zn_xMg_{1-x}O systems. We also present and compare Gaussian Process-based Bayesian Optimization models for fully automated exploration, emphasizing local reproducibility (effective noise) as an essential factor in optimal experiment workflows. Automated SPM, when coupled with upstream synthesis controls, plays a pivotal role in bridging materials synthesis and characterization.

I. Introduction

Combinatorial spread libraries are powerful tools for materials discovery. These libraries typically contain binary or ternary isothermal cross-sections of multicomponent phase diagrams, and more advanced synthesis methods can generate spatially encoded 4D and 5D compositional spaces [1]. This versatility makes them well-suited for both optimizing materials through direct exploration of compositional spaces and advancing physics discovery by exploring property and microstructure evolution [2-10]. Additionally, temperature gradients during synthesis can help reveal the effects of synthesis variables, while localized ion- or laser-based annealing enables broader exploration of the processing and chemical spaces within the selected material systems [8, 11, 12].

The first experiments in combinatorial research date back to the 1960s [13, 14], with renewed interest in the 1990s following the discovery of high-temperature superconductors [3, 4, 11, 15-17]. However, it quickly became apparent that successful combinatorial research requires not only synthesis but also detailed characterization, along with the ability to derive insights from characterization results and use these for subsequent experiment planning or transition towards different fabrication routes. Without the capacity to quantify a material's structural and functional properties as a function of composition, progress in materials discovery remains limited [18, 19]. While advances have been made in discovering materials with easily measurable optical properties [20, 21], progress in other material classes has been slower, leading to “combinatorial winters” similar to the “AI winters” in computing. Additionally, although various compositions across a selected compositional space can be generated, these often correspond to uniform synthesis conditions, while optimal synthesis parameters may vary across compositions. Furthermore, questions persist regarding the relationship between the properties observed in combinatorial libraries and those in corresponding bulk phases. Despite these challenges, multiple strategies are emerging to address these limitations, with characterization remaining the primary bottleneck.

Scanning probe microscopy (SPM) methods are exceptionally well-suited to address the challenges of characterization. Several classes of SPM techniques are intrinsically quantitative and yield information that directly correlates with functional properties of interest [22-25]. For example, piezoresponse force microscopy (PFM) allows for quantitative measurements of electromechanical responses, directly relating to piezoelectric tensor coefficients and hysteresis loop probing [26-28]. Similarly, light-induced Kelvin probe force microscopy (KPFM) can detect photovoltage—a critical aspect of photovoltaic materials functionality [29, 30]. In many cases, current- and microwave-based SPM techniques also yield quantitative data since conductivity variations in materials often exceed tip-surface contact variability and related topographic cross-talks.

Several other SPM techniques offer composition-dependent proxy signals that are closely connected to core functionalities, even if the underlying mechanisms are not fully understood. For example, electrochemical strain microscopy detects bias-induced strain, providing insights into ion concentration, molar volume, and mobility in electrochemically active materials [31-33]. Additionally, ferroelectric and ferromagnetic domain patterns serve as proxies for phase symmetry

and material disorder strength, while even simple topographic measurements can indicate growth mechanisms, phase separation, and other structural characteristics [34, 35].

However, SPM measurements are sequential and can be time intensive. Standard SPM imaging typically requires around 10 minutes per location, although faster SPM techniques are available. Spectroscopy measurements across sufficiently large grids, necessary for statistical averaging, further lengthen the process. This presents a baseline for SPM exploration of combinatorial samples. For large-scale samples, additional factors, such as instrument tuning and tip condition monitoring, can significantly increase experiment duration. Given these constraints, grid-based exploration of combinatorial libraries can take 20-30 hours even for binary cases [36], making ternary and more complex compositional spaces prohibitively time-consuming. These challenges underscore the need for machine learning (ML) algorithms to assist in controlling the microscope, tuning parameters, and selecting optimal measurement regions based on optical signals [37, 38]. Developing algorithms capable of efficiently exploring compositional spaces, especially beyond traditional grid-based searches, is particularly important.

Previously, we have demonstrated the ML algorithms for physics-based exploration of combinatorial libraries [38-41]; however, in that case selection of location was performed by human operators. More recently, we have demonstrated the automated microscopy exploration of polarization switching at single locations and grid exploration of combi libraries [36, 42]. Here, we for the first time fully operationalize the ML-controlled automated experiment in the SPM including the spectroscopy optimization and combinatorial space exploration. We demonstrate the effect of several possible Gaussian Process engines, and suggest possible benchmarking strategies for the automated SPM.

II. Decision making in automated experiment

A key aspect of autonomous exploration workflows is the transition from static ML models to active decision-making and execution on the experimental platform. In ferroelectric combinatorial library exploration, the ML agent must initiate operations such as selection of measurement location and large scale stage motion, instrument optimization in the imaging and spectroscopic modes, topographic and PFM imaging, and PFM spectroscopy at specific locations. This involves defining appropriate hyperparameters, including scan size, modulation voltage, setpoints, and spectroscopic parameters. For effective exploration across combinatorial spaces, the ML agent also requires control over probe engagement and retraction as necessary for the large-scale sample stage movement. Although not implemented here, it is worth noting that access to optical data from the instrument camera and the ability to optimize spectroscopic parameters would be essential components. For the instrument used in this study, the connections enabling these functions are described in AESPM (automated experiment on SPM) [43].

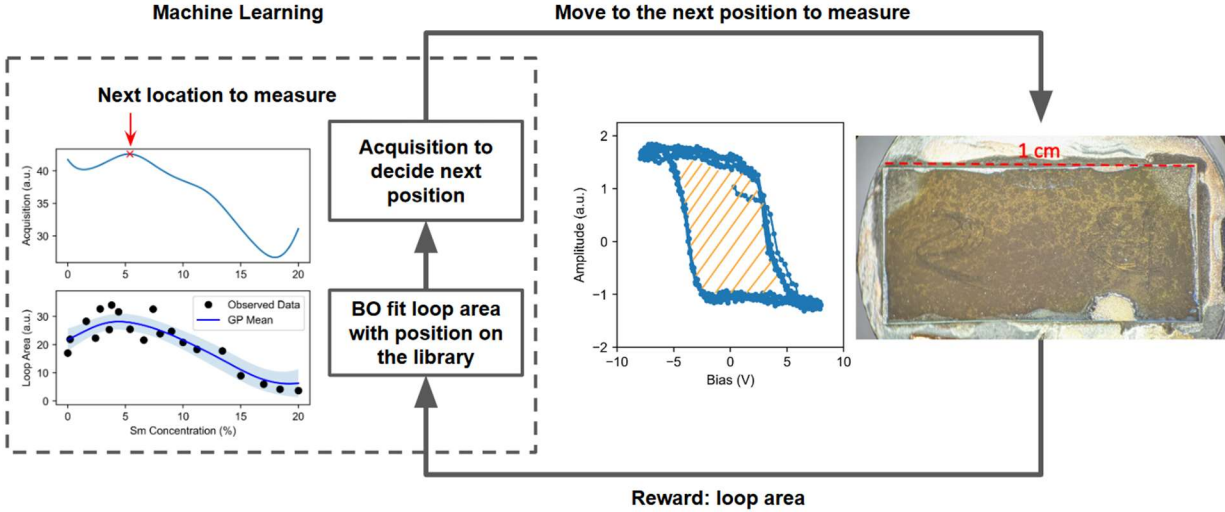


Figure 1. Workflow of autonomous exploration of a ferroelectric combinatorial library. In the autonomous exploration of a ferroelectric combinatorial library, we extract the hysteresis loop areas from the DART spectra as the reward function to represent the ferroelectric property of the library sample. During the exploration process, each iteration starts with fitting the measured loop areas and their locations of measurements with a Gaussian process (GP) model. Then an acquisition function is computed based on the prediction and uncertainty of the GP model. The next location to measure is subsequently determined based on the acquisition function and the experiment policy. The exploration process is iterated until the desired uncertainty level is achieved or the maximum number of exploration steps is reached.

A critical part of combinatorial library exploration is selecting measurement locations. The simplest strategy is grid-based exploration, where the instrument performs sequential measurements of target functionalities, moving across a uniform grid within the composition space, as encoded by sample position within the library. For more detailed characterization, compositional profiles can also be validated via chemical or X-ray analysis; however, positional encoding generally serves as the primary parameter. Unfortunately, as demonstrated by Raghavan et al. [36], grid-based exploration can be relatively slow. Additionally, changes in material properties across compositions may be compounded by factors such as tip state changes, instrument drift, and other time-dependent effects.

Decision-making for combinatorial libraries can often be myopic, as the sample state at one location generally does not depend on the sequence of prior measurements [44]. However, effective decision-making requires balancing several key considerations. The first is the discovery target—the function to be optimized or revealed. This is critical, as intrinsic measurements in SPM are often images or spectra, while optimization requires selecting one or more specific target functions. For PFM spectroscopy, these targets might include loop area, nucleation biases, or remanent polarization. The choice of reward function, or scalarizer, directly influences the progression of the automated experiment. A second, often overlooked consideration is how to handle and interpret noise. In classical Gaussian Process-Bayesian Optimization (GP-BO), noise

is accounted for through noise priors in the GP model, which are initialized before the active learning process and dynamically adjusted [38, 45, 46]. Frequently, these priors serve as hyperparameters and are fine-tuned to enhance convergence based on model behaviors that approximate experimental conditions.

However, this approach may oversimplify noise interpretation for several reasons. First, noise represents both instrumental and material sources. Instrumental noise, or system noise, can be estimated prior to the experiment and typically remains a constant component of prior system knowledge rather than an optimization hyperparameter. Second, materials themselves may exhibit spatial variability due to factors like disorder or nanoscale phase separation, leading to non-uniform properties manifested as position-dependent noise. Additionally, signal interference—such as topographic crosstalk or contamination patches—can vary across compositional space. In the systems explored here, noise variability often depends on sample location within the composition space. For instance, nanodomain formation near morphotropic phase boundaries or phase separation in solid solutions can create local inhomogeneities, resulting in sample-dependent noise increases.

To address these complexities, we use an experimental protocol in which multiple spectroscopic measurements are collected over a grid at each composition within the combinatorial library. This allows us to create a surrogate model based on the classical GP approach, using the average of measured signal for each composition. Alternatively, heteroscedastic GP models can be employed to learn noise variation across the composition space [47]. In the heteroscedastic GP, the noise is learned from multiple measurements and its spatial distribution is represented as a second independent GP. Lastly, we developed a measured noise GP model, where both the optimization function and noise are measured at each spatial location and then extrapolated to unmeasured locations using two independent GPs.

III. Autonomous exploration of Sm-BFO library

As a first model case, we explored the Sm-doped BiFeO_3 (SmBFO) combinatorial library. Here, the BFO side is ferroelectric rhombohedral material, whereas the 20% Sm-doped BFO is orthorhombic non-ferroelectric material. The intermediate concentrations are associated with the formation of the morphotropic phase boundary between crystallographically incompatible materials, often associated with enhanced piezoelectric properties. Previously we have used similar samples for a set of the electron and scanning probe microscopy studies. In particular, we used it for human-executed exploration and grid-based exploration via autonomous microscopy [36], thus providing a natural benchmark for this study.

Note that the dependence of the hysteresis loop area on concentration exhibits a non-trivial trend that went unnoticed in previous studies [36]. While we expect the simple maximum of the ferroelectric behavior at the morphotropic phase boundary, here we observe the clear two peaks. We attribute this behavior to the ease of switching of materials close to MPB, that leads to the narrowing of the hysteresis loop due to the switching effect of the Vac probing voltage [48, 49].

These studies illustrate the broad range of information that can be explored over combinatorial spaces.

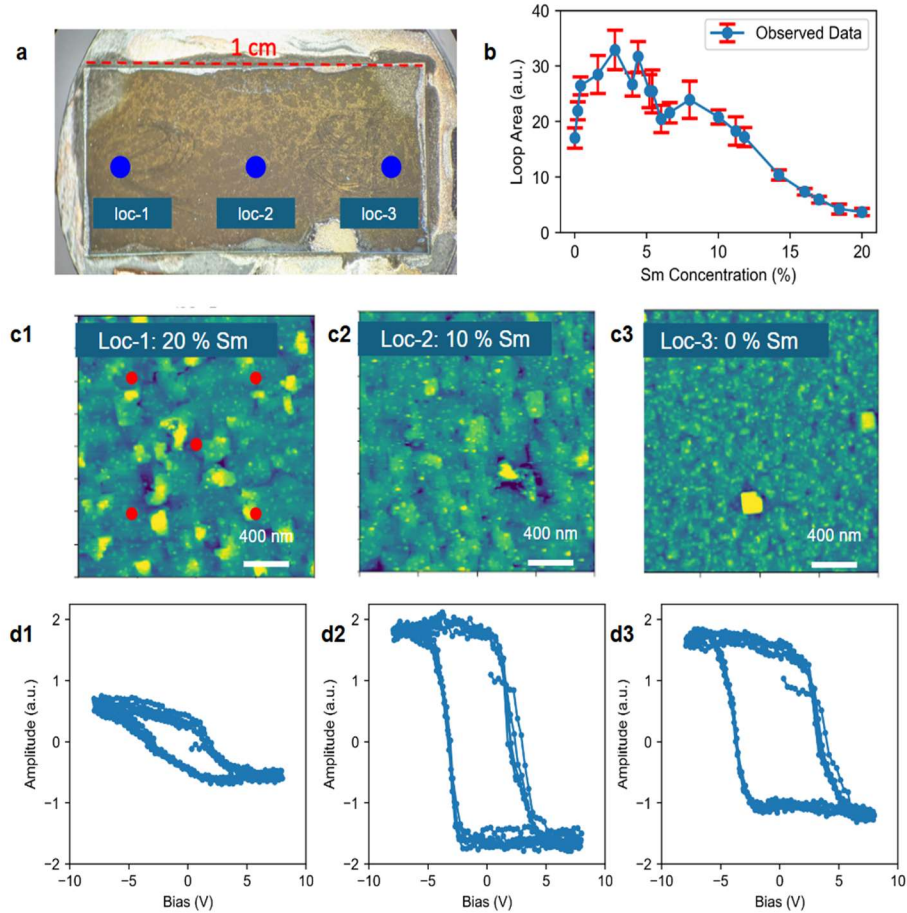


Figure 2. Overview of the combinatorial library $\text{Sm}_x\text{Bi}_{1-x}\text{FeO}_3$ (SmBFO). **a**, photo of the SmBFO combinatorial library. **b**, grid-search measurements on the SmBFO combi sample. There are 20 locations with 10 DART spectra at each location in the grid. The averaged loop areas are extracted from the DART spectra and plotted as a function of position on the library. The error bar is plotted based on the standard deviation of the loop area measured at each location. **(c1-c3)**, topography maps measured at the corresponding locations in **a**. **(d1-d3)**, typical ferroelectric amplitude hysteresis loop measured with DART at the same locations in **(c1-c3)**. The red dots in **c1** indicate the spots of DART measurement in the $2 \mu\text{m}$ map at each composition.

IV. Comparison between vBO and nBO on a grid

We first compare the performance of vBO and nBO based on grid-search data from the SmBFO library, collected at 20 locations with 10 DART spectra at each location. The 10 DART spectra are distributed over 5 spots within a $2 \mu\text{m}$ area, as shown in Figure 2-c1, providing a statistical distribution of loop areas. The main characteristics of the average loop area across the composition space shown in Figure 3a align with expected SmBFO behavior: a gradual increase

in loop area from 0 to 7-8% Sm, marking the morphotropic phase boundary (MPB) location, followed by a decline toward the non-ferroelectric composition. To establish a baseline for nBO, we use a Gaussian process (GP) model to fit loop area variations based on position, as seen in Figure 3b. More grid-search results can be found in Figure S1.

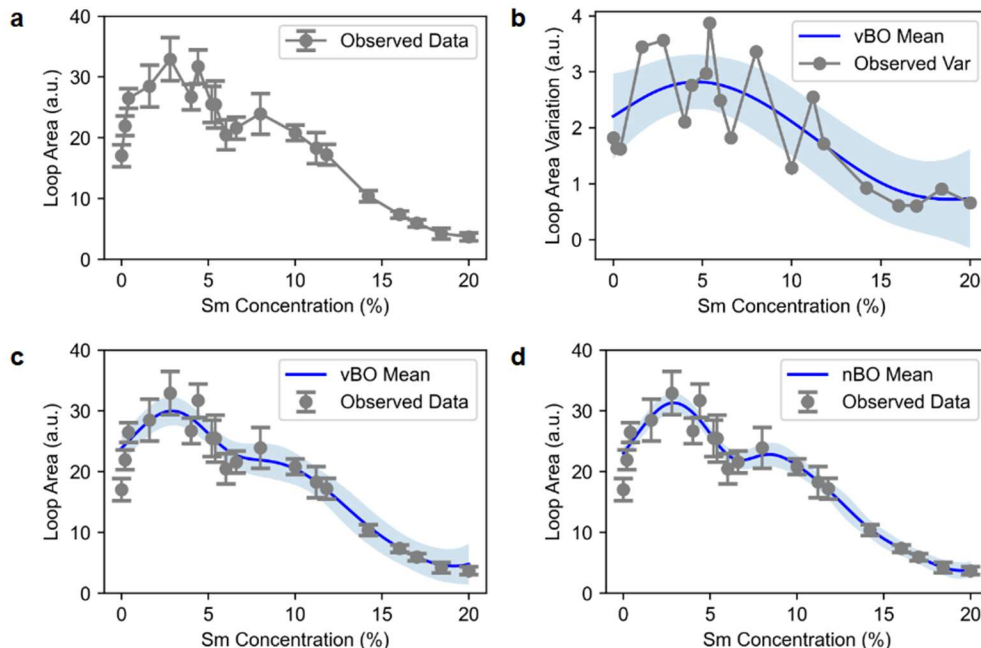


Figure 3. Comparison of vBO and nBO based on the grid-data. **a**, exploration of Sm-BFO combinatorial library on a grid. There are 20 locations on the grid. At each location, we measured 10 DART spectra at 5 spots within a $2 \mu\text{m}$ area as indicated in Figure 2c1. The averaged loop areas are plotted as a function of position and the error bar represents the standard deviation of these loop areas at each location. **b**, fitting the measured variation of loop areas as a function of positions by a GP. The confidence interval and the GP mean are plotted on top of the observed variations. **c**, GP fitting of the loop areas. In a vanilla BO, the variation of reward functions is modeled as a distribution function and is inferred only from the variation of reward functions measured at different parameters. **d**, measured noise BO fitting of the loop areas. In addition to using a GP to fit the averaged loop area as **c**, nBO employs an additional internal GP to fit the measured variation (as shown in **b**). Thus, compared to vBO, nBO has a more precise representation of the variation, which helps it make more precise and confident predictions of the reward functions.

In vanilla Bayesian Optimization (vBO), a single GP is used to fit loop areas (Figure 3c), with uncertainty or confidence intervals derived from the GP model by assuming noise as a constant distribution based on the variability of measured reward functions across locations. In contrast, measured noise Bayesian Optimization (nBO) incorporates an internal GP to fit the experimentally measured variation in reward functions alongside a GP that models the reward functions themselves as shown in Figure 3b. This approach enables nBO in Figure 3ds to make more detailed and precise predictions, as it captures a richer variation profile compared to vBO.

Consequently, nBO exhibits lower uncertainty in predictions than vBO due to its more accurate handling of measurement variability.

However, it is important to note that nBO is more susceptible to measurement outliers because it places greater trust in individual measurements compared to vBO. For instance, if an experimental outlier occurs due to contamination or topographic interference, nBO may make inaccurate predictions based on that outlier. In contrast, vBO can smooth out the impact of outliers, capturing broader trends by maintaining a larger kernel length and allowing for increased noise tolerance. While nBO generally provides more accurate predictions and captures finer details in the data, it is also more vulnerable to occasional outliers.

V. Implementation of automated exploration workflow

We implemented fully automated exploration of ferroelectric combinatorial library workflow on an Oxford Instrument Asylum Research Jupiter SPM with a fully motorized large-scale sample stage. Because the probe needs to travel large distances above the sample surface, we map out the sample height on a grid and then interpolate to get the estimated sample height across the library before the automated experiment. This sample height information is used to determine the pre-engage height before landing at a new location to avoid tip crashing.

Each new exploration step starts with withdrawing the probe to a constant safe height (here we choose $500\ \mu\text{m}$) above the sample surface to avoid tip crashing during sample movement. The next sample position to measure is determined by finding the position corresponding to the maximum in acquisition function based on GP fitting of all previously explored positions. After the sample is navigated to the next position to measure by the motorized sample stage, we first zero the cantilever deflection as the free-air deflection can change at different positions. Then the probe is moved to the pre-engage height of $100\ \mu\text{m}$ above the expected sample surface according to the interpolated sample height – position relation. After the probe is engaged on the sample surface with a setpoint deflection of $0.5\ \text{V}$, the probe will be positioned to the center of a $2\ \mu\text{m}$ scan frame to tune the probe in contact, followed by a $2\ \mu\text{m}$ dual amplitude resonance tracking (DART) PFM [50] map.

10 DART switching spectroscopy will be performed on a five-point grid in the same area as the DART PFM map, as shown in Figure2-c1. At each point on the grid, the contact tuning is repeated twice before the spectroscopy to make sure the DART can reliably track the contact resonance despite possible variations of sample topography and surface quality. Each DART spectroscopy consists of 5 full sweeping cycles, and we average the extracted reward functions of the last 4 sweeping cycles to get rid of the large resonance frequency drift effect in the first sweeping cycle. The reward at each step is calculated as the average of the rewards extracted from these 10 spectra with the minimum and maximum rewards excluded as outliers. Similarly, the standard deviation of these 10 rewards is calculated as the reward variation. Based on the rewards and their variations measured at different sample positions, we can either fit a vanilla GP or a measured noise GP to predict the distribution and uncertainty of the rewards across the whole library, and make decisions on where to measure in the next exploration step.

All the operations described above are controlled by Python script through AESPM interface with Jupiter SPM controller to ensure that the whole exploration is fully automated [43]. To make the automated exploration workflow smooth and efficient, it is critical to allocate appropriate wait time for each operation. For operations that require approximately fixed amount of time, like withdrawing the probe, stage movement, probe approaching and tuning, we tested the timing of them repeatedly and used the maximum required duration with a few extra seconds added for safety. For the operations that produce data files, such as DART PFM scans and spectroscopy, we kept monitoring the data saving folder. The next operation is triggered once a new measurement data file is saved to the disk.

VI. Compare the performance of vBO and nBO in the automated exploration of SmBFO

In our automated exploration workflow for ferroelectric combinatorial libraries, we aim to identify compositions that maximize loop area while minimizing uncertainty in the loop area-to-composition relationship across the entire library. To achieve this, we define loop area as the area enclosed by the piezoresponse amplitude–bias curves, as shown in Figure 1. The grid-search of the loop area on SmBFO is shown in Figure 2b and has been previously reported in [36].

The exploration process starts with five initial seeding measurements, randomly selected on the library. At each seeding position, we measure ten piezo response hysteresis loop spectra using DART PFM, with two measurements at each of five specified spots (red dots in Figure 2-c1). From these ten spectra, we extract ten loop areas, using the average loop area as the scalarizer and the standard deviation as the measured variation of scalarizer.

In automated exploration using vanilla Bayesian optimization (vBO), a GP model is constructed to map scalarizers to their corresponding measurement positions. Subsequently, an acquisition function based on the upper confidence bound (UCB) is computed from the GP mean and uncertainty. The next measurement position is determined by maximizing this UCB acquisition function, followed by moving the probe to the selected position. This iterative process continues with a new GP model and acquisition function trained on all acquired data. The exploration stops once the desired uncertainty level is reached or the maximum number of steps is completed.

In the measured noise Bayesian optimization (nBO) experiment, we continue to use a GP model to fit scalarizers to positions. However, instead of assuming a constant noise distribution, we add an internal GP to capture the variation of the scalarizer. This internal GP provides a noise prediction for each location. Compared to vBO, nBO incorporates experimentally measured variation as model noise, resulting in more precise predictions and improved decisions for subsequent measurement locations.

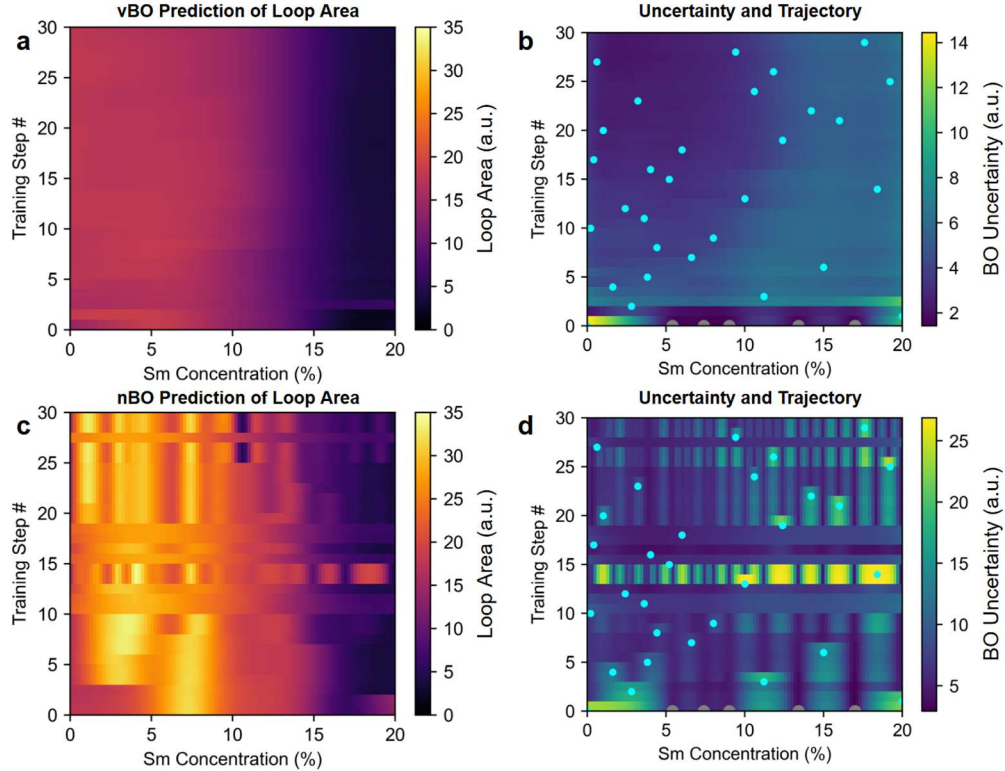


Figure 4. Exploration results of vanilla BO and measured noise BO. **a**, predicted loop area as a function of position plotted at each training step for the vanilla BO (vBO). **b**, uncertainty and trajectory of the vBO exploration. The five initial seeding locations are plotted as the gray dots at step = 0. The exploration trajectory is plotted as cyan dots. Model uncertainty is calculated as the difference between the upper and lower bounds of the BO posterior. **c-d**, predicted loop area, uncertainty and trajectory of the measured noise BO experiment. In all the three experiments, there are 5 seeding steps and 30 training steps. To minimize the uncertainty of the loop area – position relation, the acquisition of upper confidence bound (UCB) is used with $\beta = 100$.

In the vanilla Bayesian optimization (vBO) approach, the simple GP model captures the loop area-to-composition relationship with near-ideal accuracy, enabling rapid convergence. With proper seeding, the system’s essential features are identified within five steps, as evidenced by the stable predictions of loop areas after step 5 in Figure 4a. In contrast, the noise-GP model demonstrates significantly slower convergence, characterized by a rapid reduction in kernel length. Here, each local variation in the response is treated as independent of neighboring measurements, leading the algorithm to lose its ability to generalize across locations. We attribute this outcome to non-material-related factors, including surface topography variations visible in Figure 1. In this scenario, the noise signal primarily reflects surface inhomogeneity; while the simple GP smooths these variations through its kernel function, the noise GP is more susceptible to instability due to noise spikes. Although these issues can, in principle, be mitigated by adjusting kernel priors or the GP process’s mean function, the focus here is on operationalizing and benchmarking specific algorithmic approaches.

VII. Autonomous exploration of ZMO library

After we tested our auto-exploration workflow on SmBFO, we further employed our workflow to explore the ferroelectric combinatorial library $\text{Zn}_x\text{Mg}_{1-x}\text{O}$ (ZMO), a recently discovered wurtzite ferroelectric material [51]. Here instead of exploring the loop area as a function of composition, we extracted the loop height, defined as the amplitude difference at zero bias in the piezoresponse amplitude–bias curves (the red arrow in Figure 5b), as the reward. As shown in the grid-search of loop height in Figure 5c, the measured loop height shows little difference across the library.

In the automated exploration workflow, we used 5 seeding steps plus 20 exploration steps. At each step, 10 DART spectra were measured at 5 grid points in a $2\ \mu\text{m}$ area. Because ZMO has a higher coercive field compared to SmBFO, we swept the sample bias between $\pm 60\ \text{V}$ here. As shown in Figure 5d, although there were a few outliers in the beginning of the exploration, vBO was able to predict a loop height – composition relation well aligned with the grid-search results.

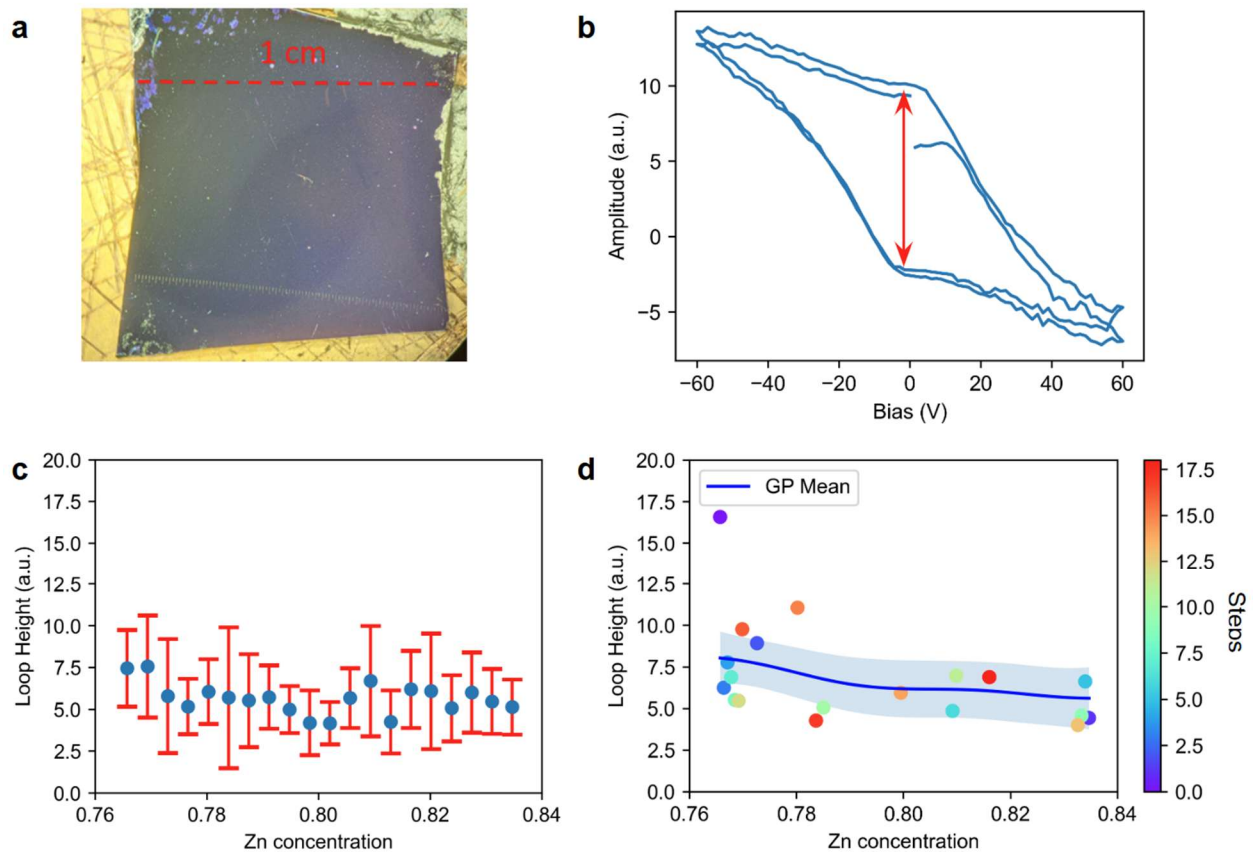


Figure 5. Automated exploration of ferroelectric loop height in $\text{Zn}_x\text{Mg}_{1-x}\text{O}$ (ZMO) combinatorial library. **a**, picture of the ZMO library. The composition variation is parallel to the red dashed line. **b**, typical piezoresponse amplitude vs. bias curve measured by DART. In this

experiment, we define the loop height as the amplitude difference at zero bias and use it as the scalarizer for the auto-exploration. **c**, grid-search of the loop height at 20 positions across the library. **d**, auto-exploration of ZMO library with vBO. Here we used 5 seeding points and 20 exploration steps.

VIII. Autonomous exploration of turn-on bias in ZMO library

As another example, we explored the turn-on bias in the ZMO library with our automated exploration experiment. As shown in Figure 6a-b, ZMO exhibits different loop sizes and shapes at different sweeping bias. Between 40 V and 50 V sweeping bias, there is a qualitative change of the phase loop as there starts showing 180-degree full phase flip. This loop opening in the phase is also accompanied by an opening in the amplitude curve in Figure 6a.

To locate the turn-on voltage precisely, we designed a binary search experiment: at each exploration step, we performed 6 DART spectra. As shown in Figure 6c, we started with an initial sweeping bias of 40 V and an initial voltage step size of 20 V. At the i -th step, the voltage step size is reduced to $20/2^{i-1}$ V, and the sign of the voltage step size is determined by whether there is a 180-degree full phase flip observed at the previous step. If we observed a 180-degree phase flip, it means that we already exceeded the turn-on voltage, so we need to reduce the sweeping bias for the next search (a “—” sign). If there is no 180-degree phase flip observed, then we will increase the sweeping bias for the next search. After 6 searching steps, the turn-on voltage can be found with a precision of 0.625 V.

In this experiment, we used vBO as the ML agent. We started with 5 seeding points and 25 exploration steps. At each step, we performed 6-step binary search at 5 locations on a grid in $2 \mu\text{m}$ area, similar to Figure 2-c1. The averaged turn-on voltage of these 5 binary search experiments is used as the reward function. We excluded the rewards greater than 75 V from the vBO fitting as this indicates that either the sample is not switchable or it requires too-high voltage to switch at that location, which is dangerous to the probe.

As shown in Figure 6d, the automated exploration experiment gives consistent turn-on voltage between 50 V and 60 V across the library.

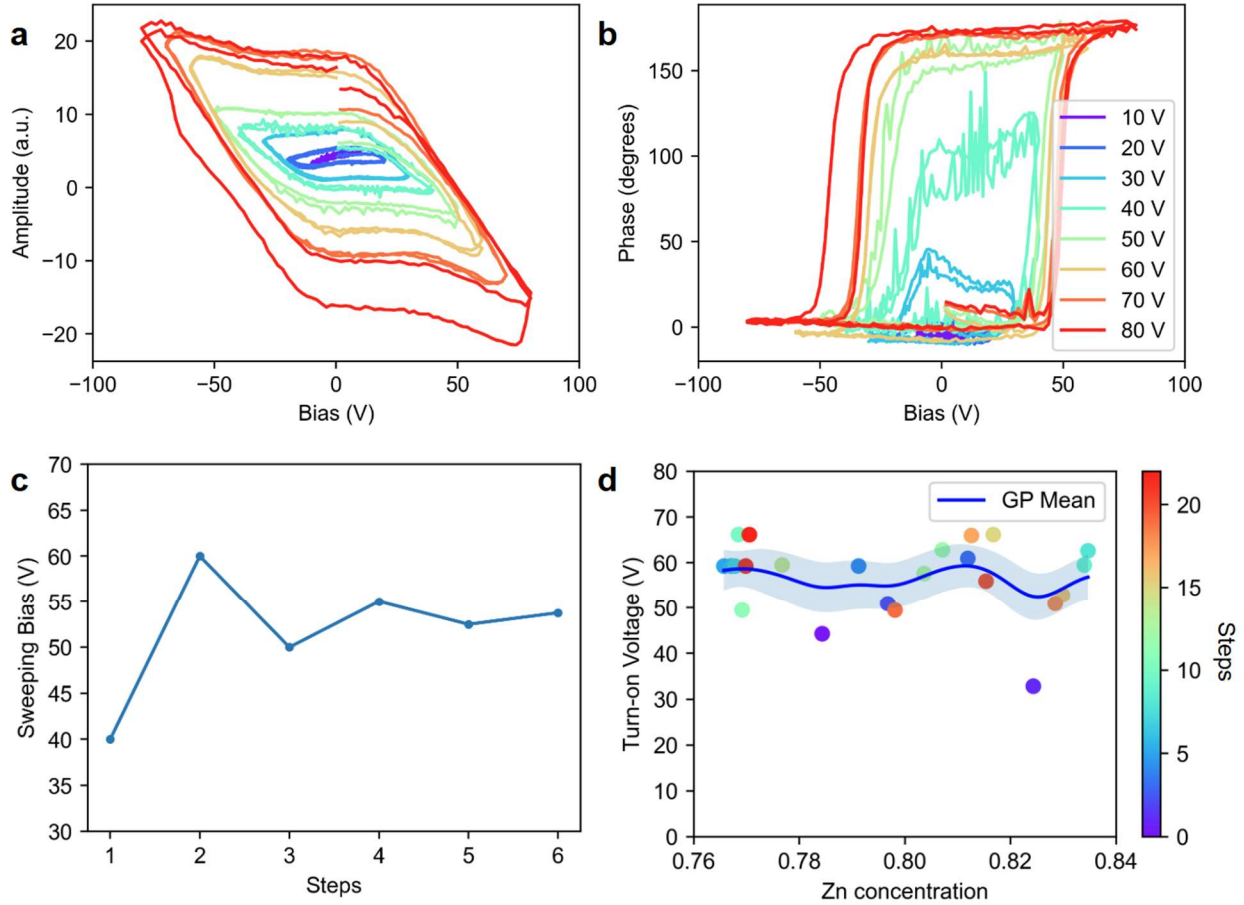


Figure 6. Automated exploration of turn-on voltage in ZMO. **a**, DART spectroscopy of piezoresponse amplitude vs. bias curves for sweeping bias ranging from 10 V to 80 V. **b**, phase vs. bias curves for the same set of DART spectra. Full switching of phase occurs between 40 V and 50 V and thus the measured turn-on voltage at this location is also between 40 and 50 V. **c**, Schematic of binary search of turn-on voltage. The search starts with an initial sweeping bias range of 40 V, and voltage step size of 20 V. At each step, the voltage step size is reduced by a factor of 2 and the direction of voltage change is determined by whether there is 180-degree phase flip in the phase curve (+ for no flip and - for flip). In this example, after 6 search steps, the turn-on voltage is found to be 53.75 V \pm 0.625 V. **d**, vBO exploration of the turn-on voltage with 6-step binary search voltage as the rewards. Here we took 5 seeding points and 25 exploration steps. The UCB acquisition function with $\beta=100$ is used to determine where to measure next at each step. We intentionally excluded the exploration points with turn-on voltage above 75 V as it indicates that either the sample is not switchable or requires too-high voltage to switch, which is dangerous to the probe.

Conclusion

PFM and, more broadly, SPM offer invaluable capabilities for exploring combinatorial material libraries. By directly detecting material functionalities and leveraging proxy signals, SPM techniques allow detailed characterization across compositional spaces. PFM, in particular, enables precise measurement of electromechanical properties, making it ideal for studying materials like ferroelectrics and piezoelectrics. These tools bridge the gap in high-resolution, quantitative data acquisition, essential for optimizing material properties in combinatorial research.

Here, we investigated multiple BO algorithms that approach noise handling and scalarization differently, showcasing the importance of tailoring these factors to enhance accuracy and efficiency. The vBO approach uses a straightforward GP model with constant noise assumptions, allowing it to generalize effectively but with limited sensitivity to local variations. In contrast, the nBO incorporates an internal GP model to capture position-dependent noise, providing finer detail in predictions but also making it more sensitive to outliers. These algorithmic comparisons underscore the impact of noise interpretation and scalarizer choice on the reliability and precision of automated SPM-based explorations.

The methodologies presented here extend beyond PFM, offering potential applications with other types of probes, such as conductive, electrochemical, and magnetic SPM. By adapting BO algorithms to different types of signals and scalarizers, this approach can be tailored to analyze various material functionalities. This flexibility is essential for advancing autonomous materials exploration across diverse combinatorial libraries and expanding the toolkit available for high-throughput characterization of complex materials. By integrating advanced SPM techniques with machine learning algorithms, this framework offers a path toward a faster materials discovery process. Automation reduces the time and labor involved in exploring vast compositional spaces, minimizing resource consumption while accelerating insights into optimal material properties. As this approach continues to develop, it has the potential to transform combinatorial materials research, driving innovation in areas like energy materials, electronic devices, and beyond.

Methods

The Sm-doped BiFeO₃ (SmBFO) thin film used in this paper was grown on SrTiO₃ substrate, with 10% Bi replaced by Sm doping. The detailed growth conditions and characterization can be found in previous publications [40, 52, 53].

The ZMO film used in this study was grown by magnetron co-sputtering at room temperature onto a platinized Si substrate. The Pt layer is 50 nm thick with a 5 nm Ti adhesion layer, both deposited by magnetron sputtering at 300 °C. The ZMO sputtering conditions are 3 mTorr total pressure with gas flows of 18 sccm Ar and 3 sccm 10%O₃/90%O₂ mix. The ZMO film thickness is 220 nm, grown at a deposition rate of 11 nm/min. The Mg/Zn ratio in the film center is approximately 30/70. Details of ZMO depositions are available in previous publications [51, 54]. Under normal deposition conditions the composition is homogeneous because of a rotating substrate with two sputter guns opposed at 180°. In the present case, the substrate rotation is turned off thus producing a linear variation in Mg:Zn ratio. EDS analysis estimates the composition variation from Mg:Zn=0.198 to Mg:Zn=0.306 across the measurement zone.

Acknowledgement

We thank Yongtao Liu for helping us take EDS measurement on the ZMO sample.

The development of automated exploration workflow of combinatorial library (YL, SVK) and growth of ZMO sample (RJS and JPM) was supported by the center for 3D Ferroelectric Microelectronics (3DFeM), an Energy Frontier Research Center funded by the U.S. Department of Energy (DOE), Office of Science, Basic Energy Sciences under Award Number DE-SC0021118.

The work at the University of Maryland (growth of SmBFO) was supported by ONR MURI N00014172661, NIST cooperative agreement 70NANB17H301, and DTRA CB11400 MAGNETO, Univ. of Maryland.

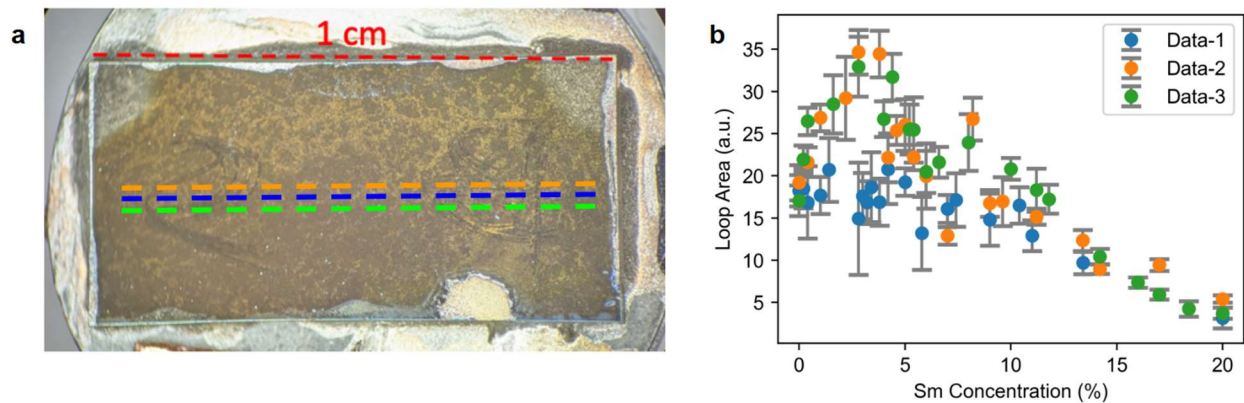


Figure S1. Grid-search of loop area on SmBFO. a, Picture of SmBFO combinatorial library showing the trajectories of three grid-search DART measurements. Each trajectory is separated by 100 μm perpendicular to the colored dashed lines in b,

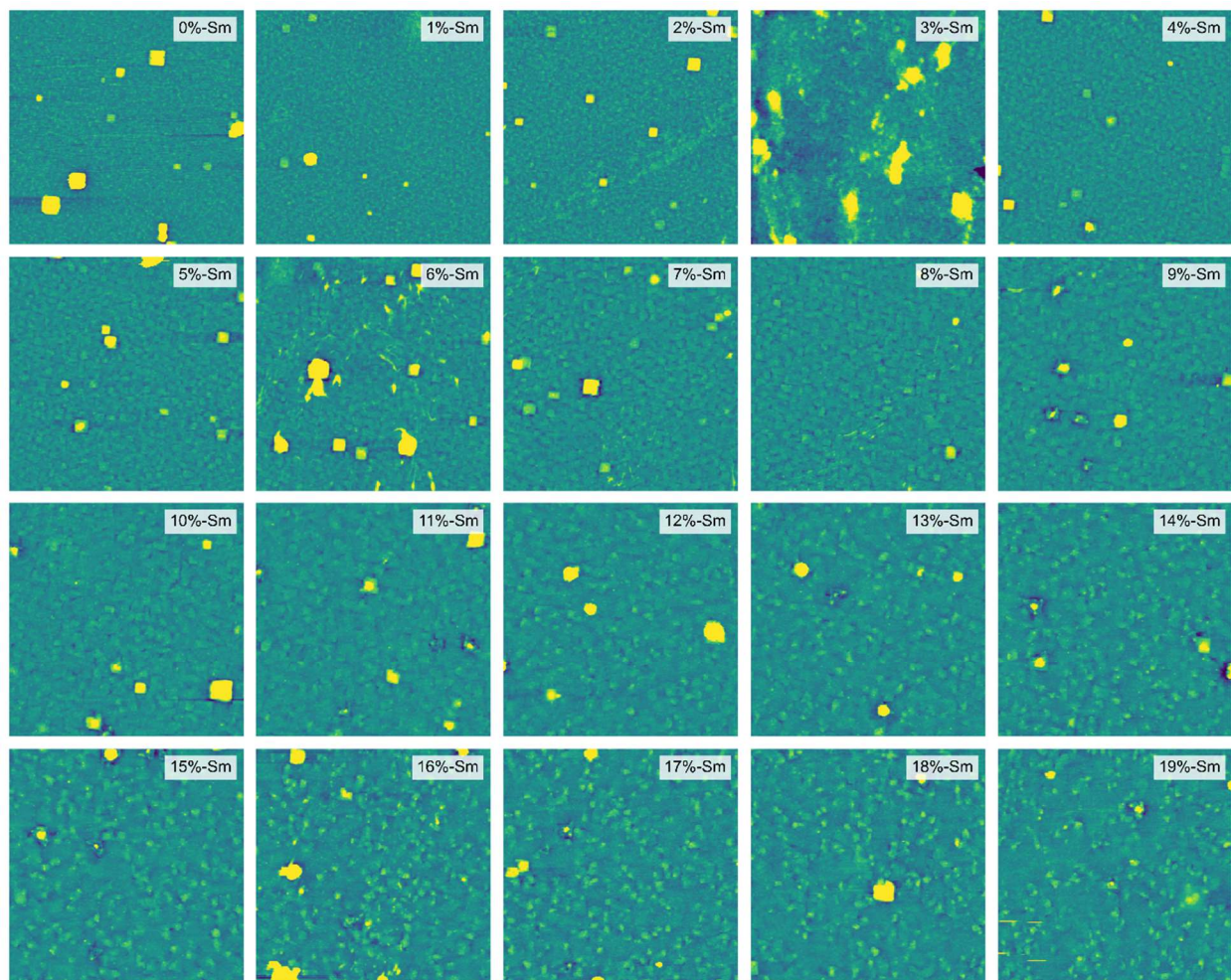


Figure S2. Grid-search of growing quality of SmBFO by topography map. 5 μm topography maps acquired on a 20-point grid across the SmBFO combinatorial library. The color scales for all the maps are kept at 26.3 nm for a comparison of sample quality at different compositions.

References

1. Lai, M., et al., *Combinatorial Synthesis and Screening of Mixed Halide Perovskite Megalibraries*. *Journal of the American Chemical Society*, 2022. **144**(30): p. 13823-13830.
2. Green, M.L., I. Takeuchi, and J.R. Hattrick-Simpers, *Applications of high throughput (combinatorial) methodologies to electronic, magnetic, optical, and energy-related materials*. *Journal of Applied Physics*, 2013. **113**(23).
3. Reddington, E., et al., *Combinatorial Electrochemistry: A Highly Parallel, Optical Screening Method for Discovery of Better Electrocatalysts*. *Science*, 1998. **280**(5370): p. 1735-1737.
4. Xiang, X.-D., et al., *A Combinatorial Approach to Materials Discovery*. *Science*, 1995. **268**(5218): p. 1738-1740.

5. Green, M.L., et al., *Fulfilling the promise of the materials genome initiative with high-throughput experimental methodologies*. Applied Physics Reviews, 2017. **4**(1).
6. Swain, B., et al., *Optimization of CdSe nanocrystals synthesis with a microfluidic reactor and development of combinatorial synthesis process for industrial production*. Chemical Engineering Journal, 2017. **308**: p. 311-321.
7. Benz, M., et al., *Marrying chemistry with biology by combining on-chip solution-based combinatorial synthesis and cellular screening*. Nature Communications, 2019. **10**(1): p. 2879.
8. Greenaway, A.L., et al., *Combinatorial Synthesis of Magnesium Tin Nitride Semiconductors*. Journal of the American Chemical Society, 2020. **142**(18): p. 8421-8430.
9. Umehara, M., et al., *Combinatorial Synthesis of Oxysulfides in the Lanthanum–Bismuth–Copper System*. ACS Combinatorial Science, 2020. **22**(6): p. 319-326.
10. Al Hasan, N.M., et al., *Combinatorial Exploration and Mapping of Phase Transformation in a Ni–Ti–Co Thin Film Library*. ACS Combinatorial Science, 2020. **22**(11): p. 641-648.
11. Koinuma, H. and I. Takeuchi, *Combinatorial solid-state chemistry of inorganic materials*. Nature Materials, 2004. **3**(7): p. 429-438.
12. Ohnishi, T., et al., *Parallel integration and characterization of nanoscaled epitaxial lattices by concurrent molecular layer epitaxy and diffractometry*. Applied Physics Letters, 2001. **79**(4): p. 536-538.
13. Boettcher, A. and R. Thun, *Phasenumwandlungen im System Kupfer—Antimon*. Zeitschrift für anorganische und allgemeine Chemie, 1956. **283**(1-6): p. 26-48.
14. Kennedy, K., et al., *Rapid Method for Determining Ternary-Alloy Phase Diagrams*. Journal of Applied Physics, 1965. **36**(12): p. 3808-3810.
15. Wang, J., et al., *Identification of a Blue Photoluminescent Composite Material from a Combinatorial Library*. Science, 1998. **279**(5357): p. 1712-1714.
16. Senkan, S.M., *High-throughput screening of solid-state catalyst libraries*. Nature, 1998. **394**(6691): p. 350-353.
17. Pullar, R.C., et al., *Dielectric measurements on a novel $Ba_{1-x}Ca_xTiO_3$ (BCT) bulk ceramic combinatorial library*. Journal of Electroceramics, 2008. **22**(1-3): p. 245-251.
18. Potyrailo, R., et al., *Combinatorial and High-Throughput Screening of Materials Libraries: Review of State of the Art*. ACS Combinatorial Science, 2011. **13**(6): p. 579-633.
19. Ludwig, A., *Discovery of new materials using combinatorial synthesis and high-throughput characterization of thin-film materials libraries combined with computational methods*. npj Computational Materials, 2019. **5**(1): p. 70.
20. Perkins, J.D., et al., *Optical analysis of thin film combinatorial libraries*. Applied Surface Science, 2004. **223**(1): p. 124-132.
21. Schenck, P.K., D.L. Kaiser, and A.V. Davydov, *High throughput characterization of the optical properties of compositionally graded combinatorial films*. Applied Surface Science, 2004. **223**(1): p. 200-205.
22. Wiesendanger, R., *Scanning probe microscopy and spectroscopy: methods and applications*. 1994: Cambridge university press.
23. García, R. and R. Pérez, *Dynamic atomic force microscopy methods*. Surface Science Reports, 2002. **47**(6): p. 197-301.
24. Dunstan, P.R., et al., *The correlation of electronic properties with nanoscale morphological variations measured by SPM on semiconductor devices*. Journal of Physics: Condensed Matter, 2003. **15**(42): p. S3095.
25. Loos, J., *The Art of SPM: Scanning Probe Microscopy in Materials Science*. Advanced Materials, 2005. **17**(15): p. 1821-1833.

26. Bonnell, D.A., et al., *Piezoresponse Force Microscopy: A Window into Electromechanical Behavior at the Nanoscale*. MRS Bulletin, 2009. **34**(9): p. 648-657.
27. Vasudevan, R.K., et al., *Spectroscopic imaging in piezoresponse force microscopy: New opportunities for studying polarization dynamics in ferroelectrics and multiferroics*. MRS Communications, 2012. **2**(3): p. 61-73.
28. Romanyuk, K., et al., *Single- and Multi-Frequency Detection of Surface Displacements via Scanning Probe Microscopy*. Microscopy and Microanalysis, 2015. **21**(1): p. 154-163.
29. Dubey, A., et al., *Mono-, Di-, and Tri-Valent Cation Doped BiFe_{0.95}Mn_{0.05}O₃ Nanoparticles: Ferroelectric Photocatalysts*. Advanced Functional Materials, 2022. **32**(43): p. 2207105.
30. Dubey, A., et al., *Lead-Free Halide Perovskites for Photocatalysis via High-Throughput Exploration*. Chemistry of Materials, 2024. **36**(5): p. 2165-2176.
31. Jesse, S., et al., *Direct Mapping of Ionic Transport in a Si Anode on the Nanoscale: Time Domain Electrochemical Strain Spectroscopy Study*. ACS Nano, 2011. **5**(12): p. 9682-9695.
32. Starr, M.B. and X. Wang, *Coupling of piezoelectric effect with electrochemical processes*. Nano Energy, 2015. **14**: p. 296-311.
33. Tavassol, H., et al., *Electrochemical stiffness in lithium-ion batteries*. Nature Materials, 2016. **15**(11): p. 1182-1187.
34. Jones, E.M.C., et al., *Reversible and Irreversible Deformation Mechanisms of Composite Graphite Electrodes in Lithium-Ion Batteries*. Journal of The Electrochemical Society, 2016. **163**(9): p. A1965.
35. Zhang, G., P. Yu, and S. Shen, *Ferroelectric-like hysteresis loops induced by chemical reaction and flexoelectricity in electrochemical strain microscopy measurements*. Journal of Applied Physics, 2018. **124**(8).
36. Raghavan, A., et al., *Evolution of Ferroelectric Properties in Sm_xBi_{1-x}FeO₃ via Automated Piezoresponse Force Microscopy across combinatorial spread libraries*. ACS Nano, 2024. **18**(37): p. 25591-25600.
37. Gormley, A.J. and M.A. Webb, *Machine learning in combinatorial polymer chemistry*. Nature Reviews Materials, 2021. **6**(8): p. 642-644.
38. Biswas, A., et al., *A dynamic Bayesian optimized active recommender system for curiosity-driven partially Human-in-the-loop automated experiments*. npj Computational Materials, 2024. **10**(1): p. 29.
39. Karniadakis, G.E., et al., *Physics-informed machine learning*. Nature Reviews Physics, 2021. **3**(6): p. 422-440.
40. Ziatdinov, M.A., et al., *Hypothesis Learning in Automated Experiment: Application to Combinatorial Materials Libraries*. Advanced Materials, 2022. **34**(20): p. 2201345.
41. Liu, Y., et al., *Explainability and human intervention in autonomous scanning probe microscopy*. Patterns, 2023. **4**(11): p. 100858.
42. Liu, Y., et al., *Disentangling Ferroelectric Wall Dynamics and Identification of Pinning Mechanisms via Deep Learning*. Advanced Materials, 2021. **33**(43): p. 2103680.
43. Liu, Y., et al., *Integration of scanning probe microscope with high-performance computing: Fixed-policy and reward-driven workflows implementation*. Review of Scientific Instruments, 2024. **95**(9).
44. Gillet, V.J., et al., *Combinatorial Library Design Using a Multiobjective Genetic Algorithm*. Journal of Chemical Information and Computer Sciences, 2002. **42**(2): p. 375-385.
45. Butler, K.T., et al., *Machine learning for molecular and materials science*. Nature, 2018. **559**(7715): p. 547-555.
46. Frazier, P.I., *Bayesian Optimization, in Recent Advances in Optimization and Modeling of Contemporary Problems*. p. 255-278.

47. Le, Q.V., A.J. Smola, and S. Canu, *Heteroscedastic Gaussian process regression*, in *Proceedings of the 22nd international conference on Machine learning*. 2005, Association for Computing Machinery: Bonn, Germany. p. 489–496.
48. Jesse, S., H.N. Lee, and S.V. Kalinin, *Quantitative mapping of switching behavior in piezoresponse force microscopy*. *Review of Scientific Instruments*, 2006. **77**(7).
49. Strelcov, E., et al., *Direct probing of charge injection and polarization-controlled ionic mobility on ferroelectric LiNbO₃ surfaces*. *Advanced Materials*, 2014. **26**(6): p. 958-963.
50. Rodriguez, B.J., et al., *Dual-frequency resonance-tracking atomic force microscopy*. *Nanotechnology*, 2007. **18**(47): p. 475504.
51. Ferri, K., et al., *Ferroelectrics everywhere: Ferroelectricity in magnesium substituted zinc oxide thin films*. *Journal of Applied Physics*, 2021. **130**(4).
52. Nelson, C.T., et al., *Deep learning ferroelectric polarization distributions from STEM data via with and without atom finding*. *npj Computational Materials*, 2021. **7**(1): p. 149.
53. Nelson, C.T., et al., *Exploring physics of ferroelectric domain walls via Bayesian analysis of atomically resolved STEM data*. *Nat Commun*, 2020. **11**(1): p. 6361.
54. Jacques, L., et al., *Wake up and retention in zinc magnesium oxide ferroelectric films*. *Journal of Applied Physics*, 2023. **133**(22).